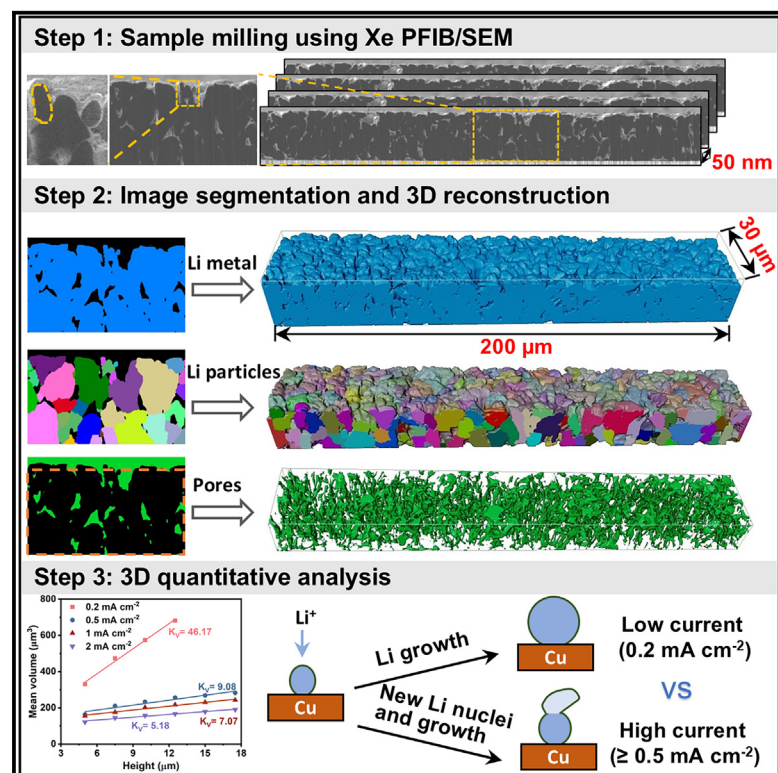


# Three-dimensional imaging of the microstructure of lithium metal anode using Xenon plasma focused ion beam

## Graphical abstract



## Authors

Yueying Peng, Kei Nishikawa

## Correspondence

nishikawa.kei@nims.go.jp

## In brief

Peng et al. employ Xenon plasma focused-ion-beam-scanning electron microscopy to visualize the 3D microstructure of large-volume electrodeposited lithium metal at high resolution. Quantitative analysis of metallic lithium, pores, and particles reveals distinct growth mechanisms at varying current densities, providing enhanced insight into lithium microstructure-performance relationships.

## Highlights

- 3D microstructure of large-volume electrodeposited Li visualized at high resolution
- Successful visualization using Xe plasma focused ion beam technology
- Study improves our understanding of Li microstructure-performance relationships
- Study provides an innovative method for electrode evaluation and optimization

## Article

# Three-dimensional imaging of the microstructure of lithium metal anode using Xenon plasma focused ion beam

Yueying Peng<sup>1</sup> and Kei Nishikawa<sup>2,3,4,\*</sup>

<sup>1</sup>International Center for Young Scientists, National Institute for Materials Science, 1-1 Namiki, Tsukuba 305-0044, Japan

<sup>2</sup>Research Center for Energy and Environmental Materials, National Institute for Materials Science, 1-1 Namiki, Tsukuba 305-0044, Japan

<sup>3</sup>Center for Advanced Battery Collaboration, Research Center for Energy and Environmental Materials, National Institute for Materials Science, 1-1 Namiki, Tsukuba 305-0044, Japan

<sup>4</sup>Lead contact

\*Correspondence: [nishikawa.kei@nims.go.jp](mailto:nishikawa.kei@nims.go.jp)

<https://doi.org/10.1016/j.xcrp.2025.102439>

## SUMMARY

The 3D microstructure of electrodeposited Li is essential for advancing Li-metal batteries because of the heterogeneous Li electrodeposition behaviors and complex phases within the electrode. However, high-resolution 3D imaging of large-scale features is challenging when using existing 3D characterization technologies. We employ Xe plasma focused-ion-beam-scanning electron microscopy for the high-resolution, large-volume 3D reconstructions of electrodeposited Li (50 nm per pixel and 200  $\mu\text{m}$  in dimension). This approach can visualize metallic Li, pores, and individual Li particles, enabling a comprehensive statistical analysis of their distribution, volume, number, and shape. We identify distinct Li growth mechanisms at low and high current densities, with Li growth being predominant at  $0.2 \text{ mA cm}^{-2}$ , while both Li growth and new nucleation occur simultaneously at  $\geq 0.5 \text{ mA cm}^{-2}$ . This study improves our understanding of Li microstructure-performance relationships and provides an innovative method for electrode evaluation and optimization.

## INTRODUCTION

The pursuit for a low-carbon, sustainable society has driven the development of advanced battery technologies. Since their commercialization in 1991, the specific energy of rechargeable lithium-ion batteries (LIBs) has improved from an initial around  $100 \text{ Wh kg}^{-1}$  to  $\sim 250 \text{ Wh kg}^{-1}$ .<sup>1,2</sup> However, current LIBs, which use a graphite anode and metal oxide cathode, are constrained by their limited theoretical energy density, which falls short of the energy storage demands of modern applications.<sup>3,4</sup> In this aspect, Li-metal batteries are considered a promising alternative. Li-metal anode offers an ultrahigh theoretical specific capacity ( $3860 \text{ mAh/g}$ , compared to  $372 \text{ mAh/g}$  for graphite) and a low redox potential ( $-3.04 \text{ V}$  vs. standard hydrogen electrode), which makes them capable of achieving significantly higher specific energy.<sup>5,6</sup> In addition, unlike graphite, which can only pair with Li-ion-containing cathodes, Li-metal can be coupled with Li-free cathodes, such as sulfur and oxygen. The theoretical specific energy of Li-S and Li-O<sub>2</sub> batteries can reach up to  $2567 \text{ Wh/kg}$  and  $3505 \text{ Wh/kg}$ , respectively.<sup>7</sup> Despite this potential, the commercial viability of Li-metal batteries is impeded by their low coulombic efficiencies (CEs), short cycle lives, and safety concerns, which stem from the highly reactive nature of Li metal and unpredictable growth of the Li microstructure.<sup>8,9</sup>

The highly reactive nature of Li metal triggers a spontaneous reaction with the electrolyte to form a solid electrolyte interphase

(SEI) layer on the surface of the metal, which results in irreversible capacity loss and electrolyte consumption.<sup>10,11</sup> During electrochemical deposition, the morphology of Li metal is uncontrollable and produces various shapes, such as whiskers, dendrites, or mossy structures.<sup>12</sup> Such high-specific-surface-area Li particles result in a Li electrode with a porous structure. This structure not only increases the risk of side reactions with the electrolyte but also tends to lose electron contact during Li stripping, which leads to rapid capacity loss and short circuits. Therefore, numerous efforts have been dedicated to controlling the morphologies of the electrodeposited Li particles to yield a compact structure, e.g., developing novel electrolytes,<sup>13</sup> designing artificial protective layers,<sup>14</sup> fabricating current collectors,<sup>15</sup> and regulating the applied external pressure.<sup>16</sup> Despite improvements in electrochemical performance, several questions remain, e.g., why specific morphologies are effective and how to realize the optimal Li structure to enhance the performance,<sup>17</sup> which poses challenges for further improvement.

Elucidating the microstructure and morphology of electrodeposited Li and their correlations with electrochemical performance is crucial for addressing this scientific challenge. First, revealing the microstructural intricacies of the Li-metal anode determined by the arrangement of the constituent phases (i.e., metallic Li and the SEI and pores) is imperative. To this end, various imaging techniques such as cryogenic transmission electron microscopy (cryo-TEM),<sup>18</sup> atomic force microscopy

(AFM),<sup>19</sup> scanning electron microscopy (SEM),<sup>20</sup> and optical microscopy,<sup>21,22</sup> have been employed. Cryo-TEM methods can capture the morphology and determine the components of the SEI at atomic resolution. SEM is commonly used for high-resolution imaging from surface and cross-sectional perspectives, offering details such as particle size and shape, surface roughness, and thickness. However, most techniques only provide 2D imaging, capturing only a single plane or cross-section, which presents inherent limitations in accurately representing the complete 3D structure. The complex 3D structure, e.g., the spatial arrangement of different phases within the Li anode and porous networks can be oversimplified when viewed using 2D imaging, thereby leading to ambiguous interpretations or incorrect conclusions considering the Li microstructure.

Characterizing the properties of active materials in the electrode, such as particle size, distribution, and shape, is crucial for understanding electrochemical performance and designing improved electrode structures.<sup>23,24</sup> Studies demonstrated that characteristics of Li particles, including their size and uniformity, have a significant effect on electrochemical performance.<sup>25–27</sup> However, because of its high reactivity, unpredictable morphology, and dynamic changes during cycling, obtaining precise quantitative information about deposited Li particles remains highly challenging. In the initial nucleation and growth stages, the sizes of the Li nuclei and nucleation density, which depend on the overpotential with a well-defined mathematical relationship, can be obtained via SEM, which provides valuable insights for enhancing the uniformity of electrodeposited Li.<sup>28,29</sup> However, more Li particles accumulate on the electrode in an overlapping stacked multilayer as electrodeposition proceeds, which renders the determination of the particle data using 2D images challenging. Consequently, quantitative data considering the sizes, distribution, and shapes of Li particles in the Li-metal electrode remain lacking.

3D imaging is indispensable for acquiring comprehensive structural data and enabling the quantitative analyses of different phases within the Li anode to overcome this limitation. However, the 3D imaging of electrodeposited Li poses several challenges. For example, Li metal displays nonuniform plating features, which leads to a heterogeneous microstructure with various Li morphologies in terms of size, distribution, and shape. The 3D structure indicates that a sufficiently large volume is necessary for reliably representing the entire electrode. A high spatial resolution image is necessary for distinguishing complex phases within the Li electrode, which includes metallic Li and the SEI and pores, and even the Li particles, if possible. 3D imaging technologies, such as X-ray computed tomography and neutron and magnetic resonance imaging, offer large-area data; however, they often struggle with low spatial resolutions or imaging contrast limitations.<sup>30–32</sup> Conversely, focused ion beam-SEM (FIB/SEM) excels in providing high-resolution images with sub-micrometer resolution, rendering it ideal for use in analyzing the detailed internal structure. Stacks of 2D images are collected via repeated FIB sequential milling to construct 3D images of a specimen, followed by SEM imaging. The resolution and volume of 3D reconstruction strongly depend on the performances of the ion sources. The Ga liquid-metal ion source is predominantly used in the FIB system because of its low melting point, volatility,

and surface free energy, excellent vacuum properties, and favorable emission characteristics.<sup>33</sup> A low beam current ranging from 1 pA to several tens of nanoamperes is used for generating a stable Ga FIB, which ensures high-quality imaging, in addition to effective nano- and micro-milling.<sup>34</sup> The Ga ion beam becomes increasingly divergent and unstable with an increase in current,<sup>35</sup> which restricts the milling depth and volume to only a few tens of microns in size.<sup>36</sup> For large-volume analysis, emerging plasma sources derived from gases, such as N<sub>2</sub>, O<sub>2</sub>, Xe, or Ar, are appealing alternatives because of their higher sputter rates. Among these, the heavier Xe ion beam exhibits the highest milling rate<sup>37</sup> and smaller spot size at a high current compared to those of the conventional Ga ion beam,<sup>38</sup> which renders it highly suitable for use in milling large-volume samples. Another attractive feature of the Xe plasma FIB (PFIB) is its lowest implantation depth compared to those of other ion sources,<sup>39</sup> which reduces the risk of material penetration and enables the production of high-quality specimens. Recently, the Xe PFIB was successfully applied to cathode electrode materials in large-scale, high-resolution characterization.<sup>40</sup> Thus far, its capacity for use in the 3D imaging of highly reactive, soft alkali metals is yet to be explored.

In this study, the 3D microstructure of electrodeposited Li, with a large volume (dimensions of 200  $\mu$ m), is successfully visualized at a high resolution (with a voxel size of 50  $\times$  50  $\times$  50 nm) using Xe PFIB technology. The electrodeposited Li metal is clearly distinguished from the surrounding components, enabling the precise quantification of its spatial distribution, packing density, and surface topography. These are crucial parameters that determine the electrochemical performance of the Li-metal anode. The proposed approach enables individually separate each electrodeposited Li particle and statistically analyzes its volume, particle number, and shape using the comprehensive dataset. These groundbreaking observations have aided in distinguishing the different growth mechanisms during electrodeposition at low and high current densities. Building on these insights, an improved understanding of the relationship between electrodeposited Li microstructures and electrochemical performances is obtained, thereby opening new avenues for developing innovative methods to design and evaluate Li-metal anodes using a novel platform.

## RESULTS

### Three-dimensional imaging using the Xe PFIB

The structure and morphology of electrodeposited Li are affected by numerous factors such as the electrolyte, applied current density, pressure, temperature, and cycle number. In this study, we used current density as a typical factor for investigating its effect on the microstructure of electrodeposited Li metal. Typical cross-sectional SEM images of electrodeposited Li, as obtained via Xe PFIB/SEM, are shown in [Figures 1A, 1B, and S1](#). These images highlight a large size of >200  $\mu$ m in the x-dimension and a high resolution with a pixel size of 50  $\times$  50 nm.

High-resolution SEM images of the well-maintained surface structure enable the clear visualization of the microstructural details of the electrodeposited Li metal. Magnified images shown in [Figure 1C](#) reveal metallic Li and the SEI and pores of the electrodeposited Li metal. The metallic Li phase comprises numerous

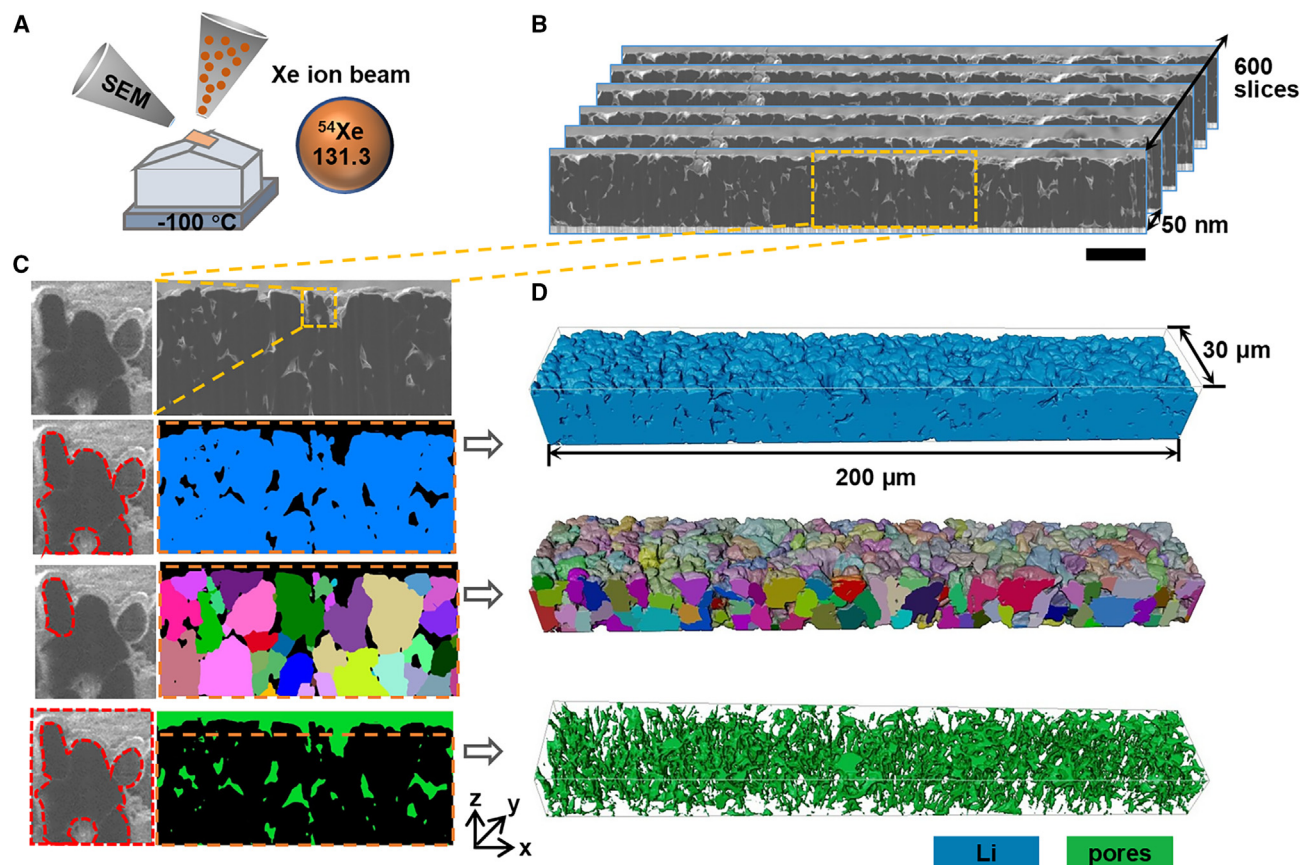


**Figure 1. Workflow used in the 3D imaging of electrodeposited Li metal using Xe PFIB/SEM**

(A) Schematic of the sample setup used in Xe PFIB/SEM.

(B) Stacks of cross-sectional SEM images of the electrodeposited Li acquired via the automatic procedure comprising Xe PFIB milling and SEM imaging. The scale bar represents 20 μm.

(C) Image segmentation of the metallic Li and pore phases; metallic Li is separated to visualize each Li particle. Magnified image of the electrodeposited Li, which shows metallic Li (black), the pores (white), and each Li particle covered by the SEI layer (thin white lines).

(D) Three-dimensional reconstruction of the Li metal (blue), separated Li particles, and inner pores (green). The volume is controlled using the same values of x = 200 μm and y = 30 μm.

Li particles, with white lines between them caused by the SEI covering layer. This separates each Li particle, and metallic Li (dark regions) can be clearly identified based on image intensity. Pore phases are generated because of voids between Li particles and surface irregularities. Inner pores can be observed when extracting volume to avoid an uneven surface. Consequently, we obtain the 3D reconstructed microstructure of electrodeposited Li, which reveals metallic Li with a clear surface topology and distinct Li particles, along with the 3D network structure of the pores, as shown in Figure 1D. These 3D microstructures enable the quantitative analysis of the electrodeposited Li based on parameters such as the area and volume fractions, surface area and curvature, volume size, and number and shapes of particles. Table S1 provides the detailed descriptions and calculations of the parameters used in this study.

#### Quantifying the metallic Li and surface topography

Figure 2A shows the reconstructed 3D images of the metallic Li phases of Li electrodeposited at current densities of 0.2, 0.5,

and 2 mA cm<sup>-2</sup>. The x and y dimensions are controlled, with the same values of 200 and 30 μm, respectively. Conversely, different z-values are attributed to the different thicknesses of the electrodeposited Li metal samples. The electrodeposited samples exhibit porous microstructures with rough, uneven surfaces. Numerous micropores are observed on the surfaces, which is consistent with SEM images showing surface views (Figure S2). A Li metal anode with a dense, compact electrode structure can be vital for reducing side reactions with the electrolyte and generation of “dead Li.” The 3D reconstructed microstructure enables the quantitative analysis of the packing density based on the Li volume and area fractions. Ideally, if the electrodeposited Li is very dense, the Li volume and area fractions should be 100%. The Li electrodeposited at 2 mA cm<sup>-2</sup> exhibits the highest Li volume fraction of 82.6%, followed by that of Li electrodeposited at 0.5 mA cm<sup>-2</sup> of 75.8%. In addition, the Li electrodeposited at 0.2 mA cm<sup>-2</sup> displays the lowest Li volume fraction of 68.7%, and notably, the lowest thickness (Figure S1). The 3D result differs from the traditional



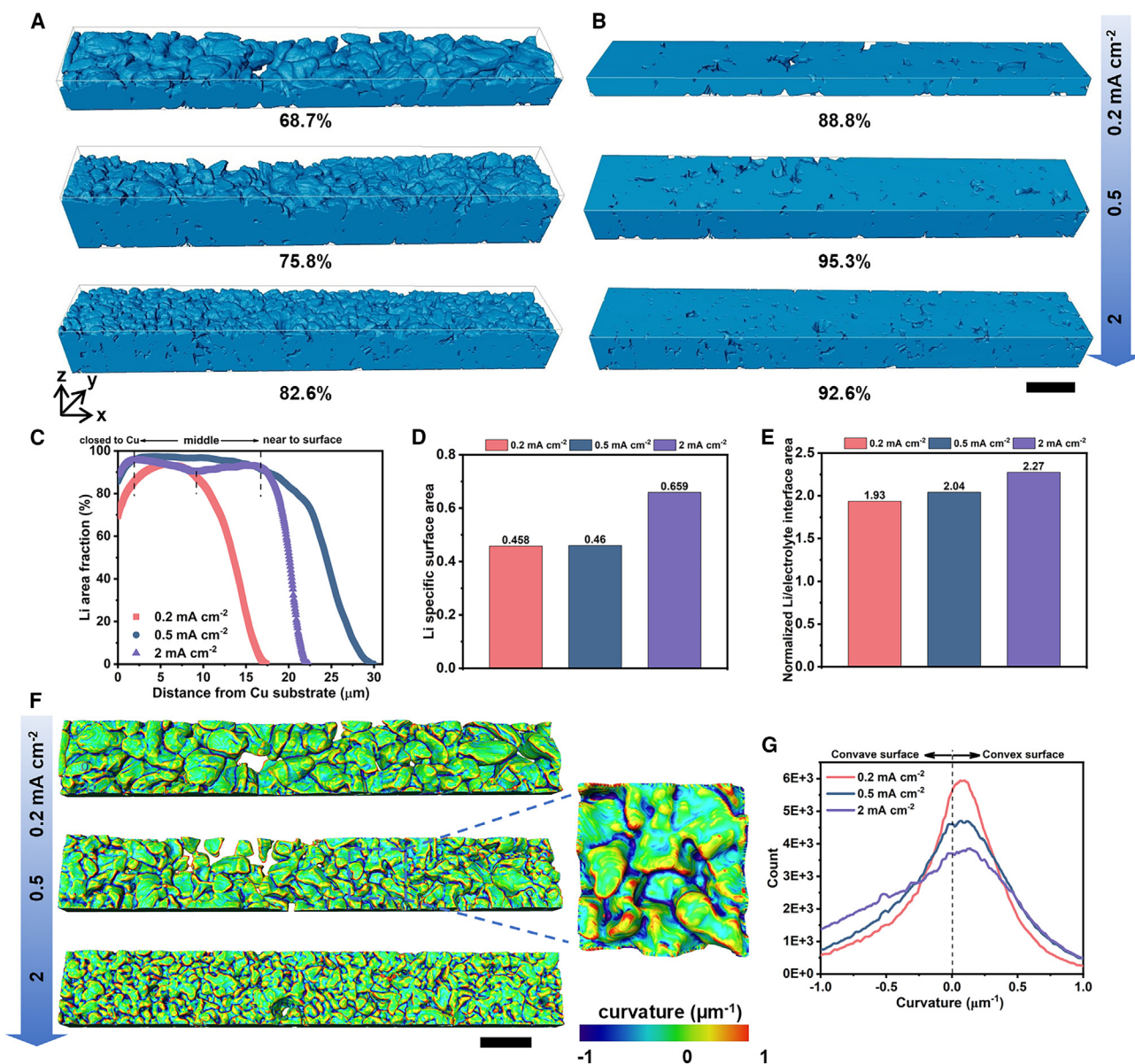


**Figure 2. Three-dimensional quantitative analyses of the metallic Li phases of electrodeposited Li electrodes**

(A and B) Reconstructed 3D images of metallic Li phases and quantified Li volume fractions of Li electrodeposited at current densities of 0.2, 0.5, and 2 mA cm<sup>-2</sup>. Reconstructed volumes (A) containing all metallic Li phases and (B) after cutting surfaces with Li area fractions of <90%. The scale bar represents 20 μm, and the volumes were controlled at same dimensions of x = 200 μm and y = 30 μm.

(C and D) Quantified data obtained from (A) for (C) Li area fractions in the xy-plane as functions of the distance from the Cu substrate and (D) Li specific surface areas.

(E–G) Quantified data obtained from generated surfaces for (E) areas of normalized Li/electrolyte interfaces, (F) surface curvature maps, and (G) corresponding quantified surface curvature distributions. The scale bar is 20 μm, and the volumes of surfaces were controlled at the same dimensions of x = 200 μm, y = 30 μm, and z = 12.5 μm.

2D understanding, where a smaller thickness indicates a denser structure. Analyzing different regions (Figure S3) indicates that the micropores significantly reduce the packing density of the Li electrode. The electrodeposited Li is uneven, which depends on the location, particularly at a low current density. The Li electrodeposited at 0.5 mA cm<sup>-2</sup> exhibits the highest Li volume fraction on reducing the effect of surface unevenness (Figure 2B and

S4). Conversely, the Li electrodeposited at a low current density of 0.2 mA cm<sup>-2</sup> consistently displays the lowest Li volume fraction. During the Li electrodeposition process, the applied charge can be consumed for both metallic Li deposition and electrolyte reduction. At low current densities, the electrodeposited Li-metal exhibits very low thickness and density, which can be attributed to increased reactions with the electrolyte. The

resulting products can either dissolve into the electrolyte or form an SEI layer on the surface.<sup>41</sup>

The cause is determined by the Li area fraction of the xy-plane along the z axis, which represents the density of metallic Li in the thickness direction, is shown in Figure 2C and Videos S1, S2, and S3. The Li area fractions of all samples gradually increase close to Cu. The distance equal to zero represents the Li/Cu contact area, which follows the order of  $2 \text{ mA cm}^{-2}$  (88.7%) >  $0.5 \text{ mA cm}^{-2}$  (85.6%) >  $0.2 \text{ mA cm}^{-2}$  (69.4%). This can be attributed to the initial nucleation density, with higher current densities resulting in higher levels of coverage via Li deposition (Figure S5). Although the Li electrodeposited at a high current density of  $2 \text{ mA cm}^{-2}$  initially exhibits a high Li area fraction, a decrease is observed in the middle region of the electrode, which is indicative of loosely packed Li particles. At a moderate current density of  $0.5 \text{ mA cm}^{-2}$ , the Li area fraction increases rapidly to  $\sim 100\%$ ; however, it decreases gradually close to the surface, which suggests a dense internal structure but an uneven surface. At a low current density of  $0.2 \text{ mA cm}^{-2}$ , the Li area fraction increases gradually in the initial stage but soon declines slightly. Therefore, generating dense Li at a low current density requires the maximization of contact with the substrate and production of a smooth surface. At a high current density, ensuring the deposition of densely packed Li particles is particularly critical.

The Li specific surface area was measured using the 3D reconstructed structure to quantify the contact area of the electrodeposited Li with the electrolyte. The surface area of Li exposed to the electrolyte is calculated using the 3D surface by normalizing over the surface area of the extracted plane (xy). Further details regarding surface generation and calculation are illustrated in Figure S6. Li electrodeposited at a high current density of  $2 \text{ mA cm}^{-2}$  exhibits a considerably higher specific surface (0.66) and normalized Li/electrolyte interfacial areas (2.27) compared to that of Li electrodeposited at 0.2 and  $0.5 \text{ mA cm}^{-2}$  (Figure 2D and 2E). This implies a higher level of contact between the metallic Li and electrolyte, increasing the risk of side reactions. Further, this result is confirmed via SEM after Li stripping, as shown in Figure S7. More residual SEI and dead Li are observed on the Cu substrate at a high current density of  $2 \text{ mA cm}^{-2}$ .

The surface geometry of the electrodeposited Li was analyzed using mean curvature (H), which indicates how a surface bends by averaging the levels of curvature in all directions. As revealed by the H mapping shown in Figure 2F, regions with H values closer to 0 (green) represent smoother surfaces. Regions with more negative H values (closer to blue) indicate more concave surfaces, which occurs in valleys between Li particles. Regions with more positive H values (closer to red) indicate more convex surfaces, which are mainly observed at contours of Li particles. Regions with high levels of curvature increase in number with an increase in current density. The specific quantitative data shown in Figure 2G reveal that the distribution of the curvature widens with an increase in current density, indicating a more uneven surface. Averaging the convex and concave surfaces, the Li electrodeposited at a low current density of  $0.2 \text{ mA cm}^{-2}$  exhibits the smallest H values (0.287 and  $-0.331$ ), followed by those of the Li electrodeposited at  $0.5 \text{ mA cm}^{-2}$  (0.327 and  $-0.349$ ). In addition, Li electrodeposited at  $0.2 \text{ mA cm}^{-2}$  displays

the largest H values (0.350 and  $-0.417$ ). Areas with high-curvature surface features are more prone to suffer from SEI fracturing and dendritic Li growth because of the stress concentration, ionic mass transfer, and electronic charge, triggering mechanical instability, and “hot spots” for excessive Li deposition.<sup>42–44</sup>

### Quantifying Li particles and pores

Li particles can be separated clearly because of the high-resolution images obtained via Xe PFIB/SEM, which provides quantitative data such as the sizes, number, distribution, and morphologies of Li particles. The 3D renderings of Li electrodeposited at current densities of 0.2, 0.5, and  $2 \text{ mA cm}^{-2}$  are shown in Figures 3A and 3B. Their internal structures along their z-axes are visualized in Videos S4, S5, and S6. The electrodeposited Li particles display significant heterogeneity in volume, shape, and distribution. The volume histograms of the Li particles are presented in Figures 3C–3E. Li particles with volumes of  $\geq 33.5 \mu\text{m}^3$  were utilized in statistical analysis, as indicated in Figure S8 and Note S1. The total number of Li particles increases in the order  $0.2 \text{ mA cm}^{-2}$  (98) <  $0.5 \text{ mA cm}^{-2}$  (431) <  $2 \text{ mA cm}^{-2}$  (524) with an increase in current density. Conversely, the mean volume of Li particles decreases in the order  $0.2 \text{ mA cm}^{-2}$  ( $738.0 \mu\text{m}^3$ ) >  $0.5 \text{ mA cm}^{-2}$  ( $317.1 \mu\text{m}^3$ ) >  $2 \text{ mA cm}^{-2}$  ( $209.3 \mu\text{m}^3$ ). The largest Li particle size at a low current density of  $0.2 \text{ mA cm}^{-2}$  reaches  $4069.5 \mu\text{m}^3$ , which is considerably larger than those obtained at current densities of  $0.5$  ( $1709.5 \mu\text{m}^3$ ) and  $2 \text{ mA cm}^{-2}$  ( $1403.0 \mu\text{m}^3$ ).

Figures 3F–3H show the volume and number percentages of Li particles with different sizes in the ranges  $\geq 1,000$ ; 800–1,000; 600–800; 400–600; 200–400; and  $33.5\text{--}200 \mu\text{m}^3$ . At a low current density of  $0.2 \text{ mA cm}^{-2}$ , large Li particles of  $\geq 1000 \mu\text{m}^3$  exhibit a very high volume percentage (58.4%), with a moderate number percentage (22.4%). Most large particles are in direct contact with the Cu substrate (Figure S9A), which indicates that they grow from the Cu substrate. The small Li particles with sizes of  $33.5\text{--}200$  and  $200\text{--}400 \mu\text{m}^3$  display high number percentages; however, they are concentrated at the edges (Figure S9B), which indicates that they manifest because of volume clipping. Li particles with sizes of  $>400 \mu\text{m}^3$  comprise 88.8% of the total volume, suggesting that the capacity is primarily used for depositing large Li particles at a low current density of  $0.2 \text{ mA cm}^{-2}$ . In contrast, at high current densities of 0.5 and  $2 \text{ mA cm}^{-2}$ , the volume and number percentages of large Li particles ( $\geq 1000 \mu\text{m}^3$ ) decrease significantly. At  $0.5 \text{ mA cm}^{-2}$ , the respective volume and number percentages are 19.1% and 4.87%, and these values decline further to 2.27% and 0.382%, respectively, at  $2 \text{ mA cm}^{-2}$ . The highest volume percentages at 0.5 and  $2 \text{ mA cm}^{-2}$  are 24.8% and 36.4%, respectively, for Li particles with sizes of  $200\text{--}400 \mu\text{m}^3$ . The trend of the number percentage is that the smaller the Li particle, the higher the number percentage is. Small Li particles ( $33.5\text{--}200 \mu\text{m}^3$ ) are distributed throughout the electrode, not only at the edges of the sampled volume (Figure S10). Most Li particles obtained at 0.5 and  $2 \text{ mA cm}^{-2}$  are located on previously deposited Li particles rather than directly contacting the Cu substrate similar to that at a lower current density of  $0.2 \text{ mA cm}^{-2}$  (Videos S7, S8, and S9). This is confirmed by the 2D images shown in Figure S11. The dependence of the specific surface area on the Li particle size is shown in Figures 3I–3K, which confirms that larger Li particles exhibit lower specific

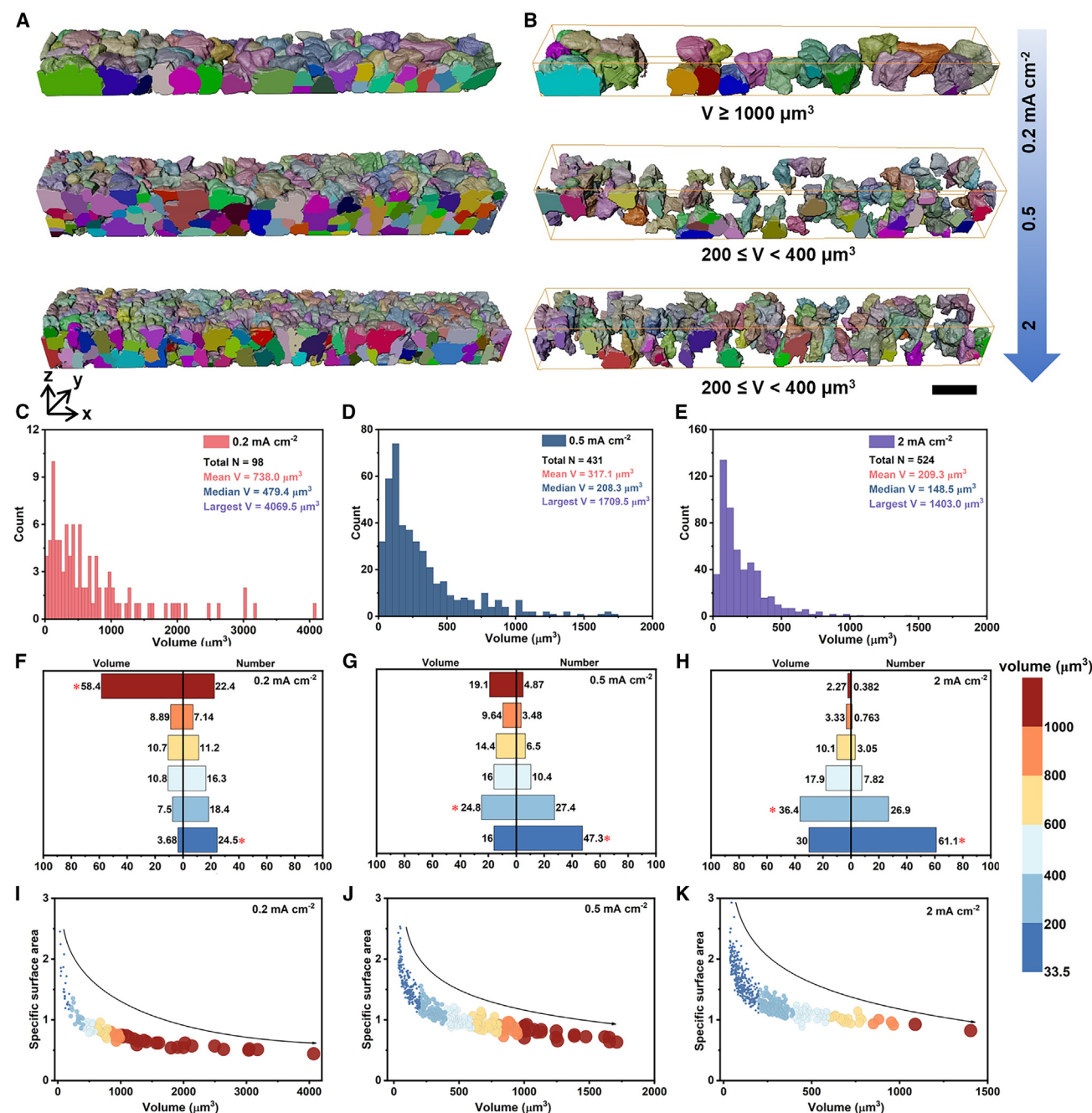


**Figure 3. Three-dimensional quantitative analyses of separated Li particles**

(A and B) Reconstructed 3D images of separated Li within the Li electrodeposited at current densities of 0.2, 0.5, and 2 mA cm<sup>-2</sup>: Reconstructed volumes containing (A) all separated Li particles and (B) Li particles within certain size ranges. The scale bar represents 20 μm, and the volumes were controlled at the same dimensions of x = 200 μm and y = 30 μm.

(C–E) Histograms of volumes and numbers of Li particles obtained at (C) 0.2, (D) 0.5, and (E) 2 mA cm<sup>-2</sup>.

(F–H) Volume and number percentages of Li particles with different sizes obtained at (F) 0.2, (G) 0.5, and (H) 2 mA cm<sup>-2</sup>.

(I–K) Dependencies of the specific surface areas of Li particles on their volumes obtained at (I) 0.2, (J) 0.5, and (K) 2 mA cm<sup>-2</sup>.

surface areas in all electrodeposited Li samples. This quantitative result confirms that forming large Li particles is advantageous for reducing their levels of contact with the electrolyte, minimizing side reactions.

In addition, the shape data of Li particles can be obtained from the 3D reconstructions of the electrodeposited Li-metal anodes using sphericity ( $\Psi$ ), which measures how closely the shape of a Li particle approaches that of a perfect sphere ( $\Psi = 1$ ). Sphericity



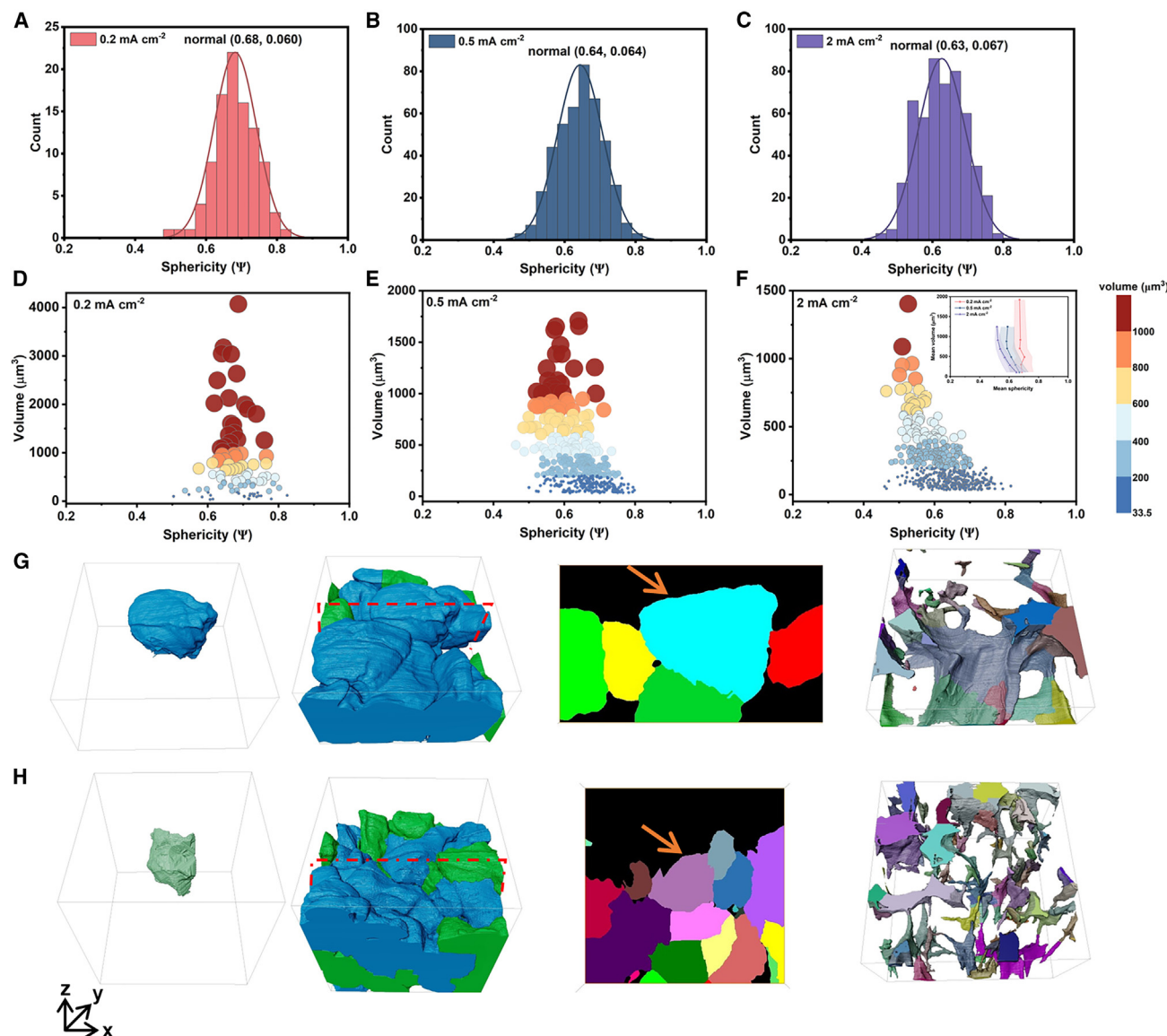


**Figure 4. Three-dimensional quantitative analyses of the shapes of separated Li particles**

(A–C) Sphericity histograms of Li particles obtained at (A) 0.2, (B) 0.5, and (C) 2 mA cm<sup>-2</sup>. The graphs display good normal distributions labeled with fitted values of (mean, variance).

(D–F) Dependencies of Li particle sphericities on their volumes at current densities of (D) 0.2, (E) 0.5, and (F) 2 mA cm<sup>-2</sup>. Inset in (F): Mean volumes as functions of mean sphericity.

(G) Analysis of an individual Li particle obtained at 0.2 mA cm<sup>-2</sup>. From left to right: One typical Li particle, its surrounding Li particles (blue particles:  $\geq 400 \mu\text{m}^3$ , green particles:  $< 400 \mu\text{m}^3$ ), a typical x-y plane slice, and separated pore structure.

(H) Analysis of an individual Li particle obtained at 0.5 mA cm<sup>-2</sup>. From left to right: one typical Li particle, its surrounding Li particles, a typical x-y plane slice, and the separated pore structure.

histograms are shown in Figures 4A–4C. The normal distribution fits well in each case, and the mean follows the order 0.2 mA cm<sup>-2</sup> (0.68) > 0.5 mA cm<sup>-2</sup> (0.64) > 2 mA cm<sup>-2</sup> (0.63). Further, the relationship between the sphericity and volume of a Li particle is analyzed in Figures 4D–4F. The Li particles obtained at a low current density of 0.2 mA cm<sup>-2</sup> exhibit high sphericities, with a concentrated distribution. Conversely, the Li particles deposited at high current densities of 0.5 and 2 mA cm<sup>-2</sup> display

decreasing sphericities with an increase in their sizes (inset of Figure 4F).

An individual Li particle and its surrounding environment are investigated to better understand the shapes of the Li particles. Figure 4G shows a typical Li particle formed at a low current density of 0.2 mA cm<sup>-2</sup>, with a respective volume and sphericity of 1258  $\mu\text{m}^3$  and 0.76. This Li particle is surrounded by large Li particles ( $\geq 400 \mu\text{m}^3$ ). Voids between Li particles are large, with a



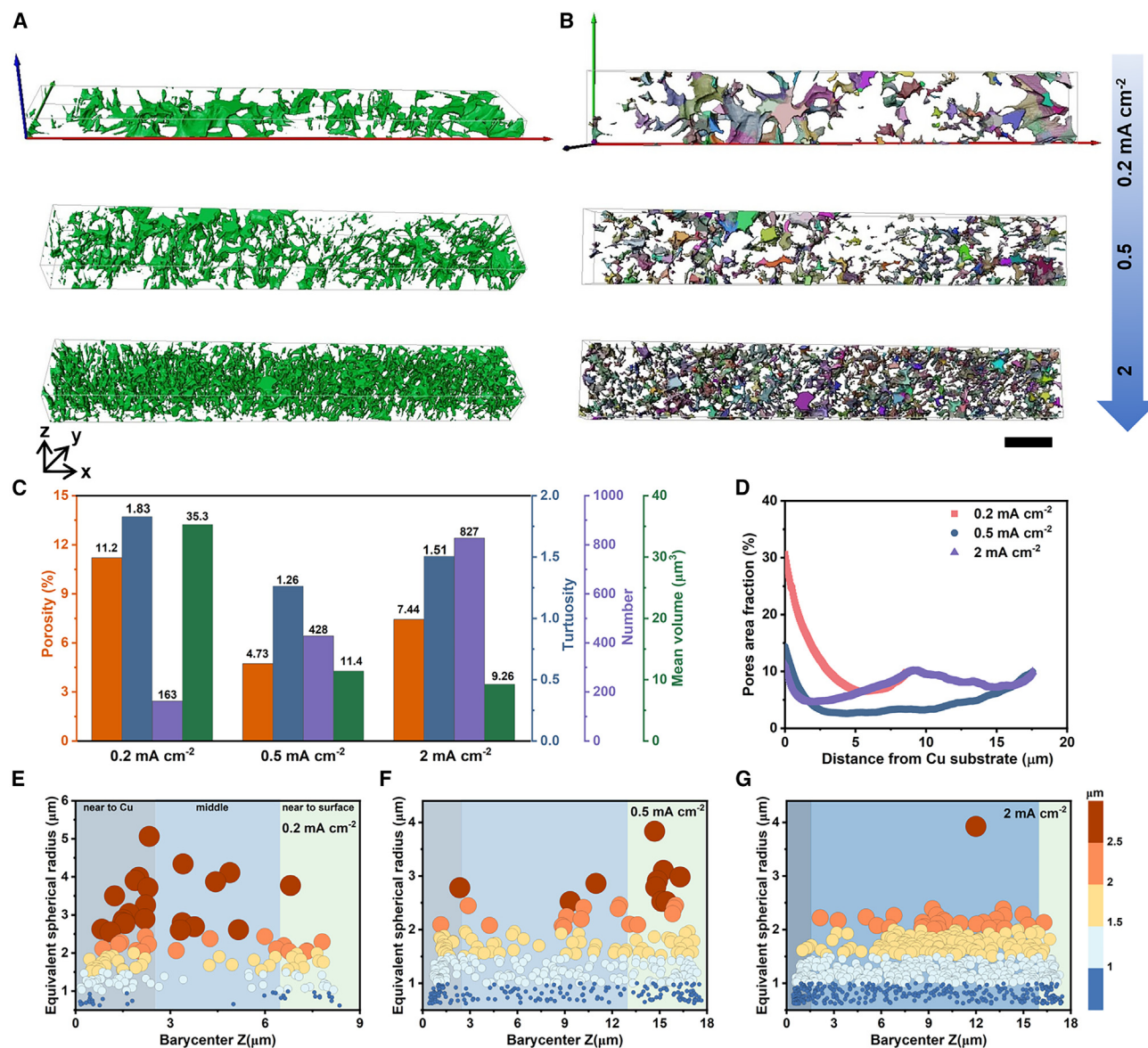


**Figure 5. Three-dimensional quantitative analyses of the pore phases of electrodeposited Li electrodes**

(A and B) Reconstructed 3D images of pore structures of electrodeposited Li obtained at current densities of 0.2, 0.5, and 2  $\text{mA cm}^{-2}$ ; (A) Reconstructed volumes of pore structures after cutting surfaces with Li volume fractions of <90% and (B) corresponding separated pore structures observed from the surface. The scale bar represents 20  $\mu\text{m}$ , and the volumes were controlled at the same dimensions of  $x = 200 \mu\text{m}$  and  $y = 30 \mu\text{m}$ .

(C) Quantified porosities, tortuosities, and numbers and mean volumes of the pores.

(D) Pore area fractions in the xy plane as functions of the distance from the Cu substrate.

(E–G) Pore size distributions in the thickness (z axis) direction obtained at current densities of (E) 0.2, (F) 0.5, and (G) 2  $\text{mA cm}^{-2}$ .

sporadic distribution. Such large pores enable Li particles to grow freely in all directions, thereby providing a good explanation for their large sizes and high sphericities. In contrast, a typical Li particle ( $404 \mu\text{m}^3$ ,  $\Psi = 0.67$ ) obtained at a high current density of 0.5  $\text{mA cm}^{-2}$  (Figure 4H) is located above another Li particle, and the generated streamlined pore structure exhibits a small size. Hence, Li particles are easily compressed by surrounding particles because of numerous particles and small pores, which grow in the direction perpendicular to the current collector.

We analyzed the structural data of pores within the electrodeposited Li electrodes to further verify this hypothesis. After removing the uneven surface regions, Figure 5A shows the reconstructed 3D images of identified pore phases obtained at current densities of 0.2, 0.5, and 2  $\text{mA cm}^{-2}$ . In addition, the corresponding separated pores are shown in Figure 5B and S12. The quantified porosities, tortuosities, and numbers and sizes of the pores are shown in Figure 5C. Li electrodeposited at 0.5  $\text{mA cm}^{-2}$  exhibit the lowest porosity (4.73%) and tortuosity

(1.26), followed by those of the Li electrodeposited at 2 (7.44%, 1.51) and 0.2 mA cm<sup>-2</sup> (11.2%, 1.83). This is consistent with the results shown in Figure 2B, which indicates that the Li inner structure with the highest density is obtained at 0.5 mA cm<sup>-2</sup>. As shown in Figure S13, the number of pores increases and the sizes of the pores decrease with an increase in current density. This result is reasonable based on results obtained for Li particles, where the number of Li particles increases, their sizes decrease, and the current density increases. In terms of the spatial positions of the pores, Figure 5D shows that the pore area fraction is initially high, and it gradually decreases with an increase in the distance from the Cu substrate. When approaching the surface, the pore area fraction increases, which is caused by spaces between the surface particles. Figures 5E–5G show the spatial distributions of the different pore sizes along the z axis. At a low current density of 0.2 mA cm<sup>-2</sup>, the pores are distributed close to the Cu substrate and surface, whereas the pores are distributed throughout the electrode at a high current density of 2 mA cm<sup>-2</sup>.

Based on these results, Li metal can grow sufficiently to form large Li particles with a lower particle number at a low current density. Pores between the Li particles are large, which promotes the growth of particles in all directions, thereby resulting in high sphericities. New Li nuclei are easily generated with an increase in the applied current density, which results in small Li particles with an increased particle number. The Li particles grow in the direction perpendicular to the current collector because of compression caused by the surrounding particles, which results in decreased sphericities.

## DISCUSSION

SEI has been demonstrated to be vital for shaping the morphology and structure of the electrodeposited Li electrode. The chemical components and structure of the SEI layer formed on the Li surface were analyzed using X-ray photoelectron spectroscopy (XPS) and cryo-scanning transmission electron microscopy/electron energy loss spectroscopy (cryo-STEM/EELS) to understand the interplay between the microstructure and SEI. XPS depth profiling was performed using initial Li samples electrodeposited at different current densities utilizing the same electrolyte comprising 4 M lithium bis(fluorosulfonyl)imide (LiFSI) in 1,2-dimethoxyethane (DME). Compared to those of the SEIs formed at high current densities of 0.5 and 2 mA cm<sup>-2</sup>, the SEI formed at 0.2 mA cm<sup>-2</sup> exhibits a lower C content and higher F, S, and N contents (Figures 6A–6C). The atomic C originates from DME reduction, whereas F, S, and N are derived from FSI<sup>-</sup> decomposition. The F/C, S/C, and N/C ratios, which represent the ratio of anion and solvent decomposition, are clearly higher at a current density of 0.2 mA cm<sup>-2</sup> (Figure 6D and S14). Therefore, anion decomposition becomes more favored than solvent decomposition with a decrease in current density. SEI rich in anion-derived products has been widely demonstrated as a superior passivated film on the Li-metal anode.<sup>45,46</sup> As shown in Figures 6E–6H and S15, the C 1s, O 1s, F 1s, S 2p, and N 1s XPS spectra are deconvoluted to further reveal the decomposed components. The surface is dominated by organic components C–C/C–H, C–O, C=O, and ROLi, which significantly decrease

after etching, thereby suggesting that organic components can occur on the outer layer of the SEI film. C–SO<sub>x</sub>, LiNSO<sub>2</sub>, NSO<sub>2</sub>, and N–SO species are distributed within the intermediate layer because their concentrations initially increase after sputtering for 1 min and then decrease upon further etching. The inorganic components Li<sub>2</sub>O, LiF, Li<sub>2</sub>S, and Li<sub>3</sub>N are detected in all samples, and their contents increase with an increase in etching time. Among these, higher amounts of LiF, Li<sub>2</sub>S, and Li<sub>3</sub>N are detected when using 0.2 mA cm<sup>-2</sup>. The SEI formed at 0.2 mA cm<sup>-2</sup> exhibits a concentrated LiF content of ~19%, which is approximately three times that observed when using 2 mA cm<sup>-2</sup> (6.1–6.8%). LiF has been extensively proven to be an effective SEI component because of its high interfacial energy, which enhances the Li-ion diffusion rate, and its high modulus, which forms a mechanically robust SEI.<sup>47,48</sup> This provides a good explanation for large Li particles with a decreased particle number at a low current density.

Cryo-STEM/EELS was also used to observe the nanostructure and components of the SEI layer. The low-magnification cryo-EM images shown in Figure 6I reveal that SEI formed at a low current density of 0.2 mA cm<sup>-2</sup> is relatively smooth compared to the rough SEI formed at 2 mA cm<sup>-2</sup> (Figure 6J). Based on the EEL spectra of the Li K-edge, peaks representing metallic Li and inorganic Li<sub>2</sub>O can be identified based on our previous study.<sup>49</sup> The thicknesses of Li<sub>2</sub>O layers formed at 0.2 and 2 mA cm<sup>-2</sup> are ~62 and 94 nm, respectively. A thicker Li<sub>2</sub>O layer suggests that more side reactions occur on the Li surface.

SEIs formed at different electrodeposition rates vary in composition and structure, which can be understood based on the reaction at the Li electrode/electrolyte interface. In the highly concentrated electrolyte (4 M LiFSI in DME), the solvated solvent molecules undergo less decomposition compared to that of free solvent molecules, which induces the formation of the anion-derived SEI layer.<sup>50</sup> During electrodeposition, solvated Li<sup>+</sup> cations diffuse and migrate to the electrode surface and undergo desolvation and reduction to metallic Li, which releases free solvent molecules. The electrodeposition reaction accelerates with an increase in current density, which leads to more desolvated solvent molecules and a thicker diffusion layer, increasing the likelihood of solvent molecules reacting with Li metal.<sup>51,52</sup> Therefore, the SEI formed at a high current density contains more species derived from solvent decomposition compared to that formed at a low current density.

The electrochemical performances of Li electrodeposited at current densities of 0.2, 0.5, and 2 mA cm<sup>-2</sup> were evaluated based on CE. Figure 7A shows Li electrodeposited at 0.5 mA cm<sup>-2</sup> exhibits the highest CE, followed by that of the Li electrodeposited at 0.2 mA cm<sup>-2</sup>. In addition, the Li electrode obtained at a high current density of 2 mA cm<sup>-2</sup> displays the lowest CE. The CEs were also compared by conducting the stripping processes at the same current density to eliminate the effect of the stripping current density (Figure 7B and S16). Yet, the electrodeposited Li obtained at 0.5 mA cm<sup>-2</sup> consistently displays the highest CE, while that obtained at 2 mA cm<sup>-2</sup> exhibits the lowest CE. The capacity loss is caused by SEI formation because of the side reaction with the electrolyte, and the generation of dead Li is caused by the loss of electrical contact with the current collector during stripping.<sup>53</sup> The results of 3D quantitative analysis reveal that Li

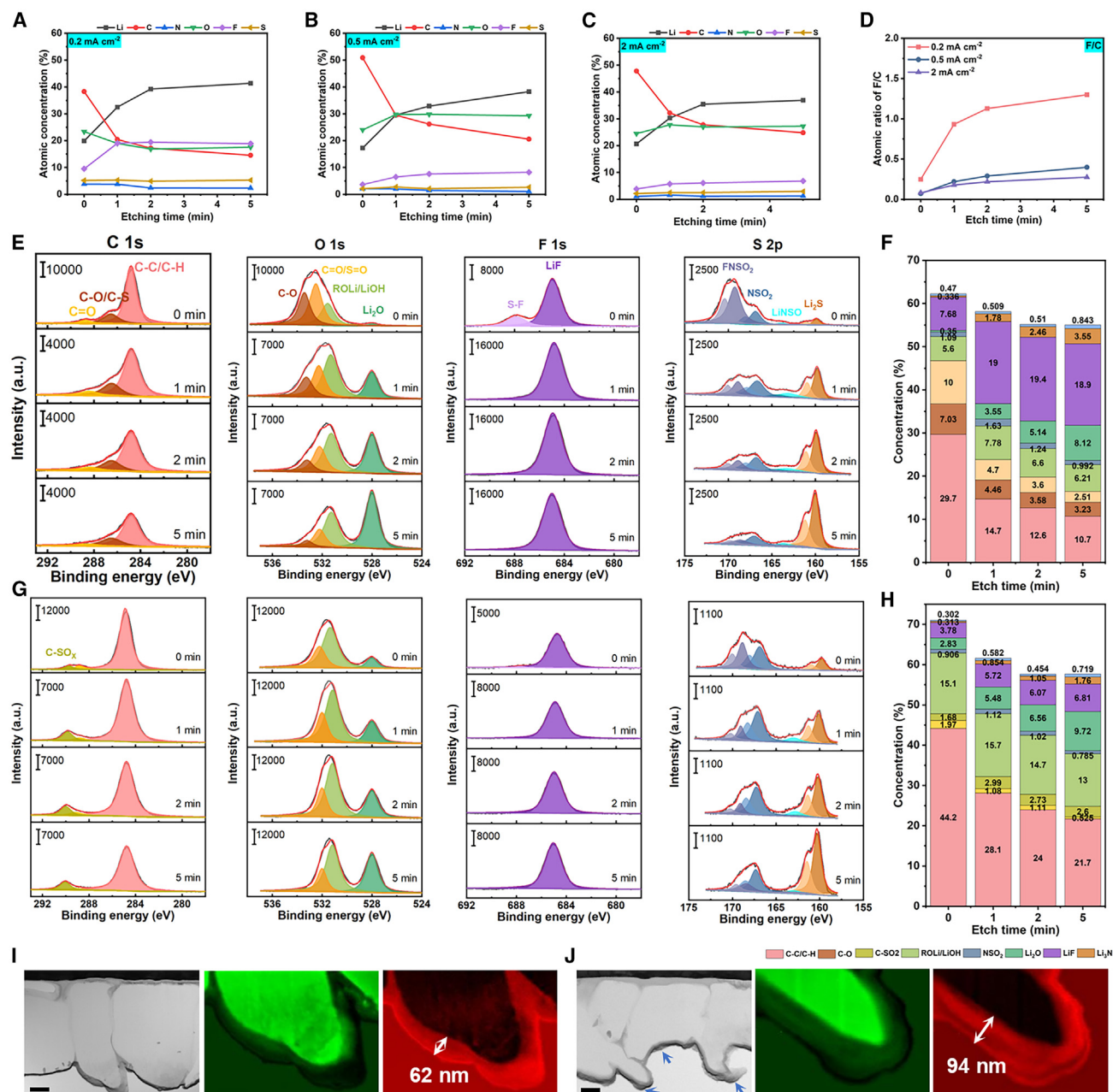


**Figure 6. Analyses of SEIs via XPS depth profiling and cryo-STEM/EELS**

(A–C) Atomic concentrations within SEIs formed at current densities of (A) 0.2, (B) 0.5, and (C) 2 mA cm<sup>-2</sup>.

(D) Atomic F/C ratios of the SEIs.

(E–H) High-resolution C 1s, O 1s, F 1s, and S 2p XPS spectra and the corresponding component concentrations of SEIs formed at current densities of (E, F) 0.2 and (G, H) 2 mA cm<sup>-2</sup>.

(I–J) TEM images and corresponding EELS maps (green and red respectively represent Li metal and Li<sub>2</sub>O) of Li electrodeposited at current densities of (I) 0.2 and (J) 2 mA cm<sup>-2</sup>. The scale bar represents 1 μm.

electrodeposited at a high current density of 2 mA cm<sup>-2</sup> suffers from severe side reactions. This can be attributed to the considerably higher Li specific surface and Li/electrolyte interfacial areas compared to those observed when using 0.2 and 0.5 mA cm<sup>-2</sup>. Further, Li particles obtained at a high current density of 2 mA cm<sup>-2</sup> exhibit a loosely packed structure with numerous

pores, smaller particle size, and increased particle number, which makes them more prone to forming dead Li. In contrast, Li electrodeposited at 0.5 mA cm<sup>-2</sup> exhibits a densely packed Li structure, promoting structural integrity and good contact with the current collector during Li stripping. The results of 3D analysis and CE evaluation demonstrate that the morphology and structure



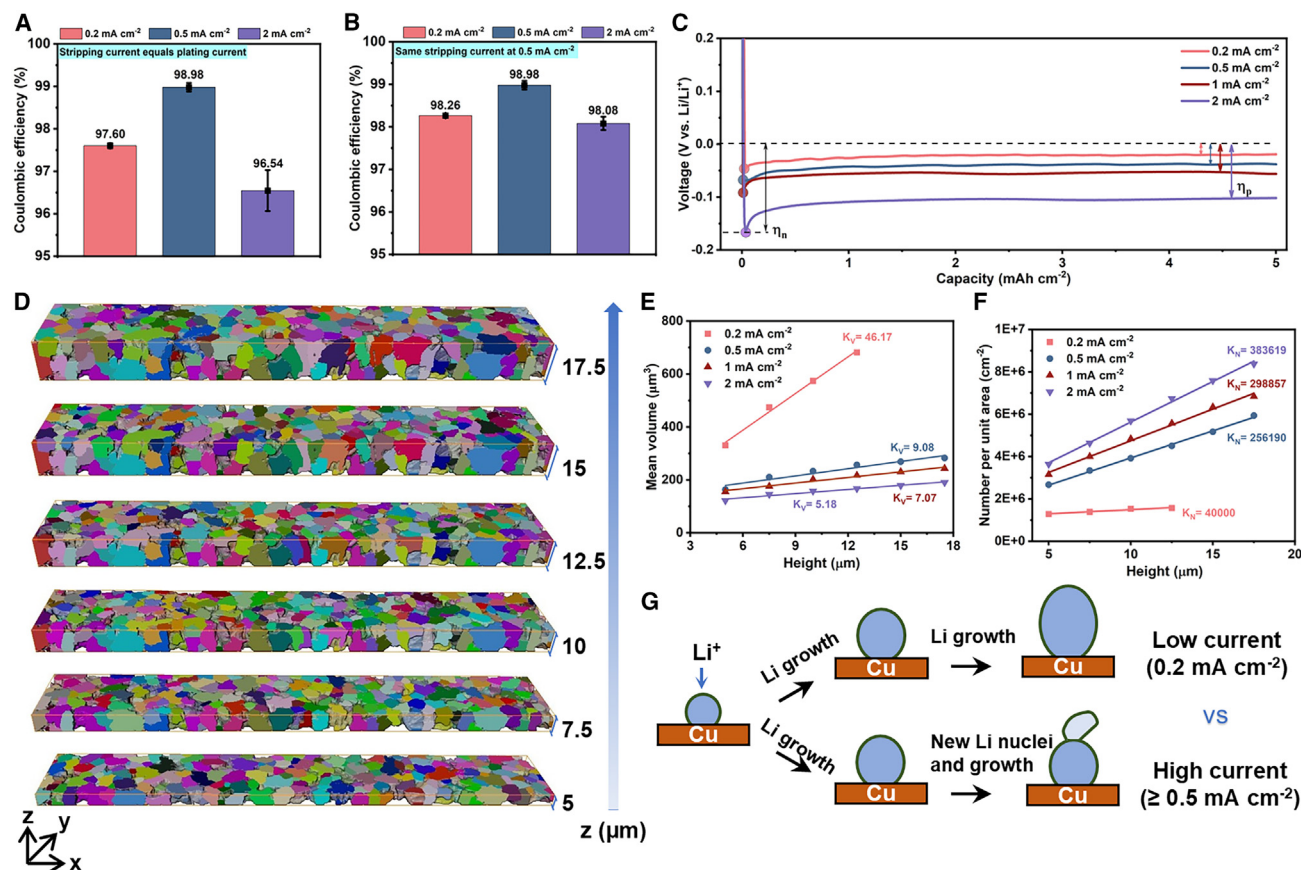


**Figure 7. Correlation of the results of 3D quantitative analysis with cell behaviors**

(A and B) CEs of Li electrodeposited at current densities of 0.2, 0.5, and 2 mA cm<sup>-2</sup> obtained using Li/Cu cells. (A) Stripping current density equals the corresponding deposition current density. (B) Stripping current density is controlled at 0.5 mA cm<sup>-2</sup>. The obtained CEs are averaged over three cells, and each error bar represents one standard deviation.

(C) Potential responses of galvanostatic Li deposition at current densities of 0.2, 0.5, 1, and 2 mA cm<sup>-2</sup>.

(D–G) Analyses of the sizes and number of Li particles during Li electrodeposition. (D) Illustration of the analyzed sub-volumes using the Li electrodeposited at 2 mA cm<sup>-2</sup> as a representative example, which gradually increases the height of the volume in the z axis direction from 5 to 7.5, 10, 12.5, 15, and 17.5 μm.

(E) Mean volumes of Li particles as functions of height, and all graphs display good linear fits labeled with fitted slopes.

(F) Numbers per area as functions of the height, and all graphs display good linear fits labeled with the fitted slopes.

(G) Schematic comparing Li growth mechanisms at different current densities.

of the Li metal generated via electrodeposition directly determine its electrochemical performance.

Another critical electrochemical parameter for assessing Li behavior is the overpotential, which reflects the magnitude of the extra potential required beyond the theoretical equilibrium potential for driving the electrodeposition reaction. Figure 7C shows the potential profiles obtained during galvanostatic Li electrodeposition at applied current densities of 0.2, 0.5, 1, and 2 mA cm<sup>-2</sup>. In typical electrodeposition, the overpotential involves the diffusion, charge transfer, reaction overpotentials, and crystallization.<sup>54,55</sup> Separating the individual contributions to the overpotential is challenging because of the simultaneous occurrence of the electrochemical processes.<sup>28,29</sup> However, two distinct regimes are evident in all cases: an initial sharp potential spike at the onset of Li deposition, which is known as the nucleation overpotential ( $\eta_n$ ), and a gradual alleviation in potential that stabilizes at a plateau ( $\eta_p$ ). The overpotential also increases

with an increase in the applied current density. As shown in Figure 7D and S17, the electrodeposited Li metal was further analyzed by incrementally increasing the height along the z axis to determine the mechanism of the electrochemical formation of Li metal. This analysis focuses on the transitions of the sizes and number of electrodeposited Li-metal particles. Figure 7E reveals the levels of the volume growth of Li-metal particles during electrodeposition. The mean volumes of Li-metal particles within the electrode volume were evaluated at intervals of 2.5 μm. A significant increase in the mean volume is only observed at 0.2 mA cm<sup>-2</sup>, whereas the increases at other current densities are relatively small. Figure 7F shows the particle number density as a function of the incremental volume of the Li-metal electrode. Further, it indicates a distinct difference at 0.2 mA cm<sup>-2</sup>: the particle number density is almost constant, in contrast to the significant increases observed under other conditions. Compared with slightly new nucleation, Li particles grow after nucleation at

a low current density. However, particle growth and new nucleation occur simultaneously at a high current density. The findings in Figure 7G indicate that the applied current density drives particle growth at  $0.2 \text{ mA cm}^{-2}$ , which is aided by the mechanically robust SEI layer. At a higher current density, the SEI layer is insufficient for accommodating the large change in volume when Li particles reach a certain size. This results in the formation of new Li nuclei, which then continues to grow on previously deposited particles. Further, this suggests that electrochemical growth dominates when the obtained overpotential ( $\eta_p$ ) is low ( $\leq 20 \text{ mV}$  at  $0.2 \text{ mA cm}^{-2}$ ), which results in large-sized Li particles with less particle numbers. However, both growth and new nucleation occur simultaneously when the obtained overpotential is higher, thereby leading to small-sized Li particles with increased particle numbers. The detailed 3D analysis aids in examining the electrochemical formation of Li metal, including its nucleation, and the findings are expected to pave the way for understanding the chemistry of Li metal.

This study employed Xe PFIB tomography to visualize the 3D microstructure of the electrodeposited Li metal with a large volume (dimensions of  $200 \mu\text{m}$ ) at a high resolution ( $50 \text{ nm}$  per pixel). The results revealed unprecedented details of the metallic Li, pores, and Li particles arranged in the microstructure, which offers enhanced insight into the interplay between the microstructure, SEI, and electrochemical performance.

The 3D images of metallic Li with a clear surface were obtained, which enables the quantification of its packing density, spatial distribution, specific surface area, and surface texture. Li electrodeposited at a moderate current density of  $0.5 \text{ mA cm}^{-2}$  consistently displayed the highest CE, followed by that of the Li electrodeposited at  $0.2 \text{ mA cm}^{-2}$ . In addition, the Li electrodeposited at  $2 \text{ mA cm}^{-2}$  exhibited the lowest CE. The 3D quantitative analysis suggested that this could be caused by the densely packed structure obtained at  $0.5 \text{ mA cm}^{-2}$ , which facilitates structural integrity during dissolution. This is in addition to its low specific surface and Li/electrolyte interfacial areas, which indicates a reduced risk of side reactions. At a low current density of  $0.2 \text{ mA cm}^{-2}$ , the electrodeposited Li exhibited lower specific surface and surface areas; however, it suffered from a lower Li volume fraction. Increasing its packing density by minimizing gaps to the substrate and reducing surface micropores was crucial to enhance the electrochemical performance of Li deposited at a low current density. At high current densities, minimizing side reactions with the electrolyte and achieving a smooth surface with reduced curvature are particularly critical to improve cell performance.

In addition, a comprehensive dataset was obtained using the large 3D volume to statistically analyze the Li particles and pores, which includes their sizes, numbers, spatial distributions, and shapes. The obtained Li particles decreased in number and increased in volume with a decrease in current density; the corresponding pores also decreased in number and increased in size. Large pores facilitated the free growth of Li particles in all directions, which results in Li particles with highly spherical morphologies and smooth surfaces. In the future, with the development of a larger database for statistical analysis, a theoretical model is expected to be established, correlating the statistical characteristics of lithium particles (e.g., volume and number)

with thermodynamic parameters such as enthalpy and entropy. In-depth XPS and cryo-STEM/EELS analyses suggested that a low current density ( $0.2 \text{ mA cm}^{-2}$ ) promoted the formation of an anion-driven SEI with a smooth structure and higher inorganic content, particularly that of LiF. This promoted the development of a mechanically robust SEI layer, which supported the formation of large Li particles. Consequently, a distinct Li electrodeposition mechanism was observed at a low current density of  $0.2 \text{ mA cm}^{-2}$ , where the current facilitated the growth of Li on previously formed nuclei. Conversely, the SEI film could not accommodate a significant volumetric expansion at a higher current density, which leads to the easier formation of new Li nuclei and an increased number of Li particles. Constructing a mechanically robust SEI layer with efficient ion transport properties is vital to achieve high-rate performance in Li-metal batteries.

This study leveraged high-resolution, large-volume 3D data and provides critical insights into the microstructure of electrodeposited Li and underlying growth mechanisms. Xe PFIB/SEM enables a reliable quantitative analysis of Li microstructures, which offers valuable guidance for optimizing Li-metal anodes by examining key factors such as electrolyte, separator, temperature and pressure. Besides, it serves as a powerful tool for understanding the underlying mechanisms governing Li-metal anode behavior, such as elucidating failure mechanisms through the structural examination of lithium electrodes across different cycle numbers. Given the inherent complexity and heterogeneity of electrodes, we believe this technique holds significant promise to advance the development of efficient electrodes in energy storage and related fields.

### Chemicals and materials

DME ( $\geq 99.9\%$ ) and HCl ( $35.0\text{--}37.0\%$ ) were purchased from Kishida Chemical (Osaka, Japan). 4 M LiFSI (Tomiya Pure Chemical Industries, Tokyo, Japan) in DME was used as the electrolyte. Li foils (thicknesses of  $200 \mu\text{m}$ ,  $\geq 99.9\%$ ) and wires (diameters of  $2 \text{ mm}$ ,  $\geq 99.9\%$ ) were purchased from Honjo Metal (Higashiosaka, Japan). Cu foil (thickness of  $20 \mu\text{m}$ ,  $\geq 99.9\%$ , Nilaco, Tokyo, Japan) was first immersed in  $0.1 \text{ M}$  HCl for ultrasonic cleaning for 5 min and rinsed sequentially with  $\text{H}_2\text{O}$ , acetone, and ethanol. This process was repeated three times to remove surface impurities, and the Cu foil was finally dried overnight in a vacuum oven at room temperature.

### Cell assembly and measurement

This study used three-electrode coin-type cells (SB7, EC Frontier, Soraku, Japan) with a controlled force of 3 kgf applied via a spring considering the effect of applied pressure on the morphology of deposited Li. Cu foil (diameter:  $14 \text{ mm}$ ), Li foil (diameter:  $14 \text{ mm}$ ), and wires (diameters:  $2 \text{ mm}$ ) were employed as the working, counter, and reference electrodes, respectively. Polyethylene film ( $20 \mu\text{m}$ ) was used as the separator, and the electrolyte comprising 4 M LiFSI in DME ( $150 \mu\text{L}$ ) was added to each cell. 4 M LiFSI in DME was selected as a representative electrolyte because it was demonstrated to be an effective electrolyte for Li-metal batteries.<sup>50</sup> Li/Cu cells were (dis)charged at  $25^\circ\text{C}$  using an electrochemical measurement system (Hokuto Denko HJ1001 SD8, Meidensha, Tokyo, Japan). Current densities of  $0.2$ ,  $0.5$ ,  $1$ , and  $2 \text{ mA cm}^{-2}$  were applied to obtain the

electrodeposited Li electrodes with fixed amounts of Li ( $Q_d = 5 \text{ mAh cm}^{-2}$ ) on Cu foils. After stripping with a cut-off potential of 1.0 V to obtain the stripping capacity ( $Q_s$ ), CE was calculated using  $CE = Q_s/Q_d \times 100\%$ . Each result was calculated using parallel experiments conducted with three cells. The cells were assembled, disassembled, washed, and dried in an Ar-filled glovebox ( $O_2$  concentration:  $<1 \text{ ppm}$ , dew point: less than  $-90^\circ\text{C}$ , a nitrogen sensor was not installed; however, Ar gas was replaced periodically for our glove box). The cycled electrodes were opened in the glovebox, soaked in DME to remove surface electrolyte, and dried in the glove box. Customized transfer vessels were used for transferring samples for further characterization without exposure to air.

### Characterization

Surface morphologies of Li after plating and stripping were observed using SEM (JSM-7800F, JEOL, Tokyo, Japan). XPS depth profiling was performed using a VersaProbe II (ULVAC-PHI, Chigasaki, Japan) at a chamber pressure of  $<10^{-8}$  torr. An Ar gun was used for sputtering samples used in depth profiling, and the high-resolution XPS spectra were calibrated using the C 1s peak at 284.8 eV. Scanning transmission electron microscopy (STEM, JEM-ARM200F, JEOL) associated with EELS (Enfinium, Gatan, Pleasanton, CA, USA) was used to obtain transmission electron microscopy (TEM) images and EELS maps at a cryogenic temperature ( $-170^\circ\text{C}$ ). Electrodeposited Li on Cu foil with a capacity of  $0.25 \text{ mAh cm}^{-2}$  was used in STEM/EELS. The FIB/SEM lift-out technique was used for TEM samples, based on our previous study.<sup>49</sup>

### PFIB/SEM and 3D reconstruction

Using 4 M LiFSI in DME as a typical electrolyte, Li metal with a fixed capacity of  $5 \text{ mAh cm}^{-2}$  was deposited on Cu foils under a controlled pressure of  $3 \text{ kgf cm}^{-2}$  at current densities of 0.2, 0.5, and  $2 \text{ mA cm}^{-2}$ . Figure 1 shows the 3D microstructure of the electrodeposited Li metal; the workflow included the setup of the Xe PFIB/SEM system, acquisition of 2D slices, image segmentation, and 3D reconstruction. The electroplated Li metal, without pre-treatment, such as sputter coating, was milled using Xe PFIB, and it was followed by SEM imaging for capturing the freshly exposed surface. A Helios 5 PFIB (Thermo Fisher Scientific, Waltham, MA, USA) was used for collecting the cross-sectional SEM images. After washing and drying, the electrodeposited Li with a capacity of  $5 \text{ mAh cm}^{-2}$  was directly mounted on the holder in a glovebox, transferred to the equipment, and fixed on the stage without exposure to air. Due to the high sensitivity of metallic Li to the electron beam, a cryogenic temperature ( $-170^\circ\text{C}$ ) was necessary for reducing the damage when using the traditional Ga ion beam to mill the Li metal.<sup>56</sup> The incapacity of the Ga ion beam for accessing high currents restricted the volume of interest to only tens of microns in size.<sup>57</sup> In addition, the surface morphology of Li metal degraded significantly because of prolonged exposure to such a low temperature.<sup>56,58</sup> In contrast, the Li metal structure and surface were maintained well at a higher temperature ( $-100^\circ\text{C}$ ) when using the Xe PFIB (Figures S18, S19, and Note S2). This was attributed to its high material removal rate of  $\sim 7 \text{ s}$  in milling Li at a beam current of 500 nA.

The stage is cooled to  $-100^\circ\text{C}$  and rotated to orient the sample surface perpendicular to the PFIB column under a high vacuum ( $\sim 10^{-5} \text{ Pa}$ ). The Cu side of the current collector was oriented toward the FIB column to best preserve the surface morphology. Each slice was spaced 50 nm apart, yielding a total of  $\sim 600$  slices via the automatic repetition of this process. A Xe ion beam was employed in cross-sectional milling. Rough milling was performed at 30 kV with an ion beam current of 2.5  $\mu\text{A}$ , followed by cross-sectional cleaning at 5 kV. In fine milling, the applied potential was 30 kV with a current of 500 nA, with each slice requiring  $\sim 7 \text{ s}$  to cut. After each slice, SEM images were captured using an ion conversion and electron detector at 2 kV and 0.8 nA. The size of the original SEM image was  $\sim 5425 \times 1292$  voxels (with a voxel size of 50 nm), which corresponded to a horizontal width of  $\sim 271 \mu\text{m}$ . Cross-sectional SEM images were automatically acquired using the Auto Slice&View (ASV5.8) software (Thermo Fisher Scientific), which resulted in the collection of 650–1,000 slices.

The obtained serial cross-sectional SEM images were then imported into the Avizo 9.0 software (Thermo Fisher Scientific) for image treatment, segmentation, and 3D reconstruction. The extracted volumes were controlled at the same dimensions in the x- (4,000 voxels, equivalent to  $200 \mu\text{m}$ ) and y-directions (600 voxels, equivalent to  $30 \mu\text{m}$ ) to better compare different samples. The intensities of the original cross-sectional SEM images were adjusted slice-by-slice using the match contrast module, which ensured that all images were within a homogeneous dynamic range. A non-local means filter was applied to reduce the noise within the images. Subsequently, two phases comprising metallic Li and the pores were distinguished based on their relative intensities. The segmented images were reconstructed into a 3D model and analyzed. Each surface was generated using the same sub-volume of  $200 \times 30 \times 12.5 \mu\text{m}$ . Label analysis was performed to obtain the data for individual particles, which included their volume3d and area3d values, equivalent spherical radii, and sphericities. The tortuosity of pores along the z-direction was calculated using the extracted pore network model. The boundary values of the input and output pressures were 130,000 and 100,000 Pa, respectively, and the fluid viscosity was set to  $0.001 \text{ Pa s}$ .

### RESOURCE AVAILABILITY

#### Lead contact

Further information and requests for resources should be directed to and will be fulfilled by the Lead Contact, Kei Nishikawa ([nishikawa.kei@nims.go.jp](mailto:nishikawa.kei@nims.go.jp)).

#### Materials availability

All unique reagents generated in this study are available from the [lead contact](#) without restriction.

#### Data and code availability

This study did not generate any datasets.

### ACKNOWLEDGMENTS

This study was supported by a grant from Japan Science and Technology Agency COI-NEXT (grant no. JPMJPF2016).



## AUTHOR CONTRIBUTIONS

Y.P. and K.N. conceived the idea. Y.P. carried out experiments and analysis and wrote the manuscript. K.N. secured funding, supervised the research, and participated in discussions and manuscript revisions. All authors contributed to the discussion and provided comments on the manuscript.

## DECLARATION OF INTERESTS

The authors declare no competing interests.

## SUPPLEMENTAL INFORMATION

Supplemental information can be found online at <https://doi.org/10.1016/j.xcrp.2025.102439>.

Received: September 18, 2024

Revised: November 28, 2024

Accepted: January 17, 2025

Published: February 10, 2025

## REFERENCES

- Linden, D. (1995). *Handbook of batteries*. *Fuel Energy Abstr.* 4, 265.
- Masias, A. (2018). Lithium-ion battery design for transportation. *Fuel Energy Abstr.* 4, 1–33. <https://doi.org/10.1109/ICCCNT51525.2021.9580169>.
- Dunn, B., Kamath, H., and Tarascon, J.-M. (2011). Electrical energy storage for the grid: A battery of choices. *Science* 334, 928–935. <https://doi.org/10.1126/science.1212741>.
- Tarascon, J.-M., and Armand, M. (2001). Issues and challenges facing rechargeable lithium batteries. *Nature* 414, 359–367. <https://doi.org/10.1038/35104644>.
- Liu, B., Zhang, J.-G., and Xu, W. (2018). Advancing lithium metal batteries. *Joule* 2, 833–845. <https://doi.org/10.1016/j.joule.2018.03.008>.
- Lin, D., Liu, Y., and Cui, Y. (2017). Reviving the lithium metal anode for high-energy batteries. *Nat. Nanotechnol.* 12, 194–206. <https://doi.org/10.1038/nnano.2017.16>.
- Bruce, P.G., Freunberger, S.A., Hardwick, L.J., and Tarascon, J.M. (2011). Li-O<sub>2</sub> and Li-S batteries with high energy storage. *Nat. Mater.* 11, 19–29. <https://doi.org/10.1038/nmat3191>.
- Cheng, X.B., Zhang, R., Zhao, C.Z., and Zhang, Q. (2017). Toward safe lithium metal anode in rechargeable batteries: A review. *Chem. Rev.* 117, 10403–10473. <https://doi.org/10.1021/acs.chemrev.7b00115>.
- Fang, C., Wang, X., and Meng, Y.S. (2019). Key issues hindering a practical lithium-metal anode. *Trends Chem.* 1, 152–158. <https://doi.org/10.1016/j.trechm.2019.02.015>.
- Peled, E. (1979). The electrochemical behavior of alkali and alkaline earth metals in nonaqueous battery systems—the solid electrolyte interphase model. *J. Electrochem. Soc.* 126, 2047–2051. <https://doi.org/10.1149/1.2128859>.
- Aurbach, D., Zinigrad, E., Cohen, Y., and Teller, H. (2002). A short review of failure mechanisms of lithium metal and lithiated graphite anodes in liquid electrolyte solutions. *Solid state ion* 148, 405–416. [https://doi.org/10.1016/S0167-2738\(02\)00080-2](https://doi.org/10.1016/S0167-2738(02)00080-2).
- Frenck, L., Sethi, G.K., Maslyn, J.A., and Balsara, N.P. (2019). Factors that control the formation of dendrites and other morphologies on lithium metal anodes. *Front. Energy Res.* 7, 115. <https://doi.org/10.3389/fenrg.2019.00115>.
- Zhang, G., Chang, J., Wang, L., Li, J., Wang, C., Wang, R., Shi, G., Yu, K., Huang, W., Zheng, H., et al. (2023). A monofluoride ether-based electrolyte solution for fast-charging and low-temperature non-aqueous lithium metal batteries. *Nat. Commun.* 14, 1081. <https://doi.org/10.1038/s41467-023-36793-6>.
- Zhang, Q.-K., Zhang, X.-Q., Wan, J., Yao, N., Song, T.-L., Xie, J., Hou, L.-P., Zhou, M.-Y., Chen, X., Li, B.-Q., et al. (2023). Homogeneous and mechanically stable solid–electrolyte interphase enabled by trioxane-modulated electrolytes for lithium metal batteries. *Nat. Energy* 8, 725–735. <https://doi.org/10.1038/s41560-023-01275-y>.
- Kim, J.-M., Jia, H., Koirala, K.P., Liu, D., Simmons, A., Engelhard, M.H., Ahmed, R.A., Zhang, Y., Wang, C., Zhang, J.-G., and Xu, W. (2024). Three-dimensional polymeric-scaffold-based current collector for a lithium metal anode toward high-energy-density batteries. *ACS Energy Lett.* 9, 919–926. <https://doi.org/10.1021/acsenergylett.3c02752>.
- Fang, C., Lu, B., Pawar, G., Zhang, M., Cheng, D., Chen, S., Ceja, M., Dour, J.-M., Musrock, H., Cai, M., et al. (2021). Pressure-tailored lithium deposition and dissolution in lithium metal batteries. *Nat. Energy* 6, 987–994. <https://doi.org/10.1038/s41560-021-00917-3>.
- Wood, K.N., Noked, M., and Dasgupta, N.P. (2017). Lithium metal anodes: Toward an improved understanding of coupled morphological, electrochemical, and mechanical behavior. *ACS Energy Lett.* 2, 664–672. <https://doi.org/10.1021/acsenergylett.6b00650>.
- Li, Y., Li, Y., Pei, A., Yan, K., Sun, Y., Wu, C.L., Joubert, L.M., Chin, R., Koh, A.L., Yu, Y., et al. (2017). Atomic structure of sensitive battery materials and interfaces revealed by cryo-electron microscopy. *Science* 358, 506–510. <https://doi.org/10.1126/science.aam6014>.
- Shen, C., Hu, G., Cheong, L.Z., Huang, S., Zhang, J.G., and Wang, D. (2017). Direct observation of the growth of lithium dendrites on graphite anodes by operando EC-AFM. *Small Methods* 2, 1700298. <https://doi.org/10.1002/smt.201700298>.
- Nagao, M., Hayashi, A., Tatsumisago, M., Kanetsuku, T., Tsuda, T., and Kuwabata, S. (2013). In situ SEM study of a lithium deposition and dissolution mechanism in a bulk-type solid-state cell with a Li<sub>2</sub>S–P<sub>2</sub>S<sub>5</sub> solid electrolyte. *Phys. Chem. Chem. Phys.* 15, 18600–18606. <https://doi.org/10.1039/c3cp51059j>.
- Nishikawa, K., Mori, T., Nishida, T., Fukunaka, Y., Rosso, M., and Homma, T. (2010). In situ observation of dendrite growth of electrodeposited Li metal. *J. Electrochem. Soc.* 157, A1212. <https://doi.org/10.1149/1.3486468>.
- Wood, K.N., Kazyak, E., Chadwick, A.F., Chen, K.H., Zhang, J.G., Thornton, K., and Dasgupta, N.P. (2016). Dendrites and pits: Untangling the complex behavior of lithium metal anodes through operando video microscopy. *ACS Cent. Sci.* 2, 790–801. <https://doi.org/10.1021/acscentsci.6b00260>.
- Zhang, J., Qiao, J., Sun, K., and Wang, Z. (2022). Balancing particle properties for practical lithium-ion batteries. *Particuology* 61, 18–29. <https://doi.org/10.1016/j.partic.2021.05.006>.
- Akbar, A., Weng, J., Zhang, X., Li, P., Ye, G., and Zhou, X. (2024). Impact of active particle in lithium-ion battery probed by a microstructure resolved model. *Ind. Eng. Chem. Res.* 63, 8971–8982. <https://doi.org/10.1021/acs.iecr.4c00473>.
- Mehdi, B.L., Stevens, A., Qian, J., Park, C., Xu, W., Henderson, W.A., Zhang, J.G., Mueller, K.T., and Browning, N.D. (2016). The impact of Li grain size on coulombic efficiency in Li batteries. *Sci. Rep.* 6, 34267. <https://doi.org/10.1038/srep34267>.
- Kim, J.S., and Yoon, W.Y. (2004). Improvement in lithium cycling efficiency by using lithium powder anode. *Electrochim. Acta* 50, 531–534. <https://doi.org/10.1016/j.electacta.2003.12.071>.
- Thenuwara, A.C., Shetty, P.P., and McDowell, M.T. (2019). Distinct nanoscale interphases and morphology of lithium metal electrodes operating at low temperatures. *Nano Lett.* 19, 8664–8672. <https://doi.org/10.1021/acs.nanolett.9b03330>.
- Pei, A., Zheng, G., Shi, F., Li, Y., and Cui, Y. (2017). Nanoscale nucleation and growth of electrodeposited lithium metal. *Nano Lett.* 17, 1132–1139. <https://doi.org/10.1021/acs.nanolett.6b04755>.
- Biswal, P., Stalin, S., Kludze, A., Choudhury, S., and Archer, L.A. (2019). Nucleation and early stage growth of Li electrodeposits. *Nano Lett.* 19, 8191–8200. <https://doi.org/10.1021/acs.nanolett.9b03548>.

30. Sadd, M., Xiong, S., Bowen, J.R., Marone, F., and Matic, A. (2023). Investigating microstructure evolution of lithium metal during plating and stripping via operando X-ray tomographic microscopy. *Nat. Commun.* **14**, 854. <https://doi.org/10.1038/s41467-023-36568-z>.
31. Hao, S., Bailey, J.J., Iacoviello, F., Bu, J., Grant, P.S., Brett, D.J.L., and Shearing, P.R. (2020). 3D imaging of lithium protrusions in solid-state lithium batteries using X-ray computed tomography. *Adv. Funct. Mater.* **31**, 2007564. <https://doi.org/10.1002/adfm.202007564>.
32. Sun, F., Zieles, L., Markötter, H., Hilger, A., Zhou, D., Moroni, R., Zengerle, R., Thiele, S., Banhart, J., and Manke, I. (2016). Morphological evolution of electrochemically plated/stripped lithium microstructures investigated by synchrotron X-ray phase contrast tomography. *ACS Nano* **10**, 7990–7997. <https://doi.org/10.1021/acsnano.6b03939>.
33. Giannuzzi, L.A. (2004). Introduction to Focused Ion Beams: Instrumentation, Theory, Techniques and Practice (Springer Science & Business Media). <https://doi.org/10.1007/b10190.7990>.
34. Bassim, N., Scott, K., and Giannuzzi, L.A. (2014). Recent advances in focused ion beam technology and applications. *MRS Bull.* **39**, 317–325. <https://doi.org/10.1557/mrs.2014.52>.
35. Forbest, R. (1997). Understanding how the liquid-metal ion source works. *Vacuum* **48**, 85–97. [https://doi.org/10.1016/S0042-207X\(96\)00227-8](https://doi.org/10.1016/S0042-207X(96)00227-8).
36. Burnett, T.L., Kelley, R., Winiarski, B., Contreras, L., Daly, M., Gholinia, A., Burke, M.G., and Withers, P.J. (2016). Large volume serial section tomography by Xe Plasma FIB dual beam microscopy. *Ultramicroscopy* **161**, 119–129. <https://doi.org/10.1016/j.ultramic.2015.11.001>.
37. Berger, C., Dumoux, M., Glen, T., Yee, N.B.Y., Mitchels, J.M., Patáková, Z., Darrow, M.C., Naismith, J.H., and Grange, M. (2023). Plasma FIB milling for the determination of structures in situ. *Nat. Commun.* **14**, 629. <https://doi.org/10.1038/s41467-023-36372-9>.
38. Smith, N.S., Skoczylas, W.P., Kellogg, S.M., Kinion, D.E., Tesch, P.P., Sutherland, O., Aanesland, A., and Boswell, R.W. (2006). High brightness intensity coupled plasma source for high current focused ion beam applications. *J. Vacuum Sci. Technol. B: Microelectron. Nanometer Struct. Process. Measure. Phenomena* **24**, 2902–2906. <https://doi.org/10.1116/1.2366617>.
39. Eder, K., Bhatia, V., Qu, J., Van Leer, B., Dutka, M., and Cairney, J.M. (2021). A multi-ion plasma FIB study: Determining ion implantation depths of Xe, N, O and Ar in tungsten via atom probe tomography. *Ultramicroscopy* **228**, 113334. <https://doi.org/10.1016/j.ultramic.2021.113334>.
40. Zhang, M., Chouchane, M., Shojaei, S.A., Winiarski, B., Liu, Z., Li, L., Pelapur, R., Shodiev, A., Yao, W., Doux, J.-M., et al. (2023). Coupling of multi-scale imaging analysis and computational modeling for understanding thick cathode degradation mechanisms. *Joule* **7**, 201–220. <https://doi.org/10.1016/j.joule.2022.12.001>.
41. Geise, N.R., Kasse, R.M., Nelson Weker, J., Steinrück, H.-G., and Toney, M.F. (2021). Quantification of efficiency in lithium metal negative electrodes via operando X-ray diffraction. *Chem. Mater.* **33**, 7537–7545. <https://doi.org/10.1021/acs.chemmater.1c02585>.
42. Park, J., Jeong, J., Lee, Y., Oh, M., Ryou, M.H., and Lee, Y.M. (2016). Micro-patterned lithium metal anodes with suppressed dendrite formation for post lithium-ion batteries. *Adv. Mater. Interfaces* **3**, 1600140. <https://doi.org/10.1002/admi.201600140>.
43. Harry, K.J., Higa, K., Srinivasan, V., and Balsara, N.P. (2016). Influence of electrolyte modulus on the local current density at a dendrite tip on a lithium metal electrode. *J. Electrochem. Soc.* **163**, A2216–A2224. <https://doi.org/10.1149/2.0191610jes>.
44. Cho, J.H., Kim, K., Chakravarthy, S., Xiao, X., Rupp, J.L.M., and Sheldon, B.W. (2022). An investigation of chemo-mechanical phenomena and lithium metal penetration in all-solid-state lithium metal batteries using in situ optical curvature measurements. *Adv. Energy Mater.* **12**, 2200369. <https://doi.org/10.1002/aenm.202200369>.
45. Oyakhire, S.T., Zhang, W., Holmes, S.E., Sayavong, P., Kim, S.C., Boyle, D.T., Kim, M.S., Zhang, Z., Cui, Y., and Bent, S.F. (2023). Correlating the formation protocols of solid electrolyte interphases with practical performance metrics in lithium metal batteries. *ACS Energy Lett.* **8**, 869–877. <https://doi.org/10.1021/acsenenergylett.2c02137>.
46. Peng, Y., Nishikawa, K., and Kanamura, K. (2022). Effects of carbonate solvents and lithium salts in high-concentration electrolytes on lithium anode. *J. Electrochem. Soc.* **169**, 060548. <https://doi.org/10.1149/1945-7111/ac797a>.
47. Shin, H., Park, J., Han, S., Sastry, A.M., and Lu, W. (2015). Component-/structure-dependent elasticity of solid electrolyte interphase layer in Li-ion batteries: Experimental and computational studies. *J. Power Sources* **277**, 169–179. <https://doi.org/10.1016/j.jpowsour.2014.11.120>.
48. Liu, Y., Tao, X., Wang, Y., Jiang, C., Ma, C., Sheng, O., Lu, G., and Lou, X.W.D. (2022). Self-assembled monolayers direct a LiF-rich interphase toward long-life lithium metal batteries. *Science* **375**, 739–745. <https://doi.org/10.1126/science.abn1818>.
49. Nishikawa, K., and Shinoda, K. (2021). Characterization of electrodeposited Li metal by cryo-scanning transmission electron microscopy/electron energy loss spectroscopy. *J. Phys. Chem. Lett.* **12**, 3922–3927. <https://doi.org/10.1021/acs.jpcclett.1c00717>.
50. Qian, J., Henderson, W.A., Xu, W., Bhattacharya, P., Engelhard, M., Borodin, O., and Zhang, J.G. (2015). High rate and stable cycling of lithium metal anode. *Nat. Commun.* **6**, 6362. <https://doi.org/10.1038/ncomms7362>.
51. Kamesui, G., Nishikawa, K., Ueda, M., and Matsushima, H. (2022). Mass transfer during electrodeposition and dissolution of Li metal within highly concentrated electrolytes. *ACS Energy Lett.* **7**, 4089–4097. <https://doi.org/10.1021/acsenenergylett.2c02120>.
52. Miki, A., Nishikawa, K., Kamesui, G., Matsushima, H., Ueda, M., and Rosso, M. (2021). In situ interferometry study of ionic mass transfer phenomenon during the electrodeposition and dissolution of Li metal in solvate ionic liquids. *J. Mater. Chem. A* **9**, 14700–14709. <https://doi.org/10.1039/d1ta02666f>.
53. Fang, C., Li, J., Zhang, M., Zhang, Y., Yang, F., Lee, J.Z., Lee, M.H., Alvarado, J., Schroeder, M.A., Yang, Y., et al. (2019). Quantifying inactive lithium in lithium metal batteries. *Nature* **572**, 511–515. <https://doi.org/10.1038/s41586-019-1481-z>.
54. Vetter, K.J., and Barnatt, S. (1968). Electrochemical kinetics: Theoretical aspects. *J. Electrochem. Soc.* **115**, 262Ca. <https://doi.org/10.1149/1.2411429>.
55. Winand, R. (1991). Electrocrystallization: Fundamental considerations and application to high current density continuous steel sheet plating. *J. Appl. Electrochem.* **21**, 377–385. <https://doi.org/10.1007/BF01024572>.
56. Lee, J.Z., Wynn, T.A., Schroeder, M.A., Alvarado, J., Wang, X., Xu, K., and Meng, Y.S. (2019). Cryogenic focused ion beam characterization of lithium metal anodes. *ACS Energy Lett.* **4**, 489–493. <https://doi.org/10.1021/acsenenergylett.8b02381>.
57. Cantoni, M., and Holzer, L. (2014). Advances in 3D focused ion beam tomography. *MRS Bull.* **39**, 354–360. <https://doi.org/10.1557/mrs.2014.54>.
58. Yang, Y., Davies, D.M., Yin, Y., Borodin, O., Lee, J.Z., Fang, C., Olguin, M., Zhang, Y., Sablina, E.S., Wang, X., et al. (2019). High-efficiency lithium-metal anode enabled by liquefied gas electrolytes. *Joule* **3**, 1986–2000. <https://doi.org/10.1016/j.joule.2019.06.008>.